

Research Article

Design and Analysis of a Novel Piezo-Actuated $XY\theta_z$ Micropositioning Mechanism with Large Travel and Kinematic Decoupling

Ruijiang Xiao ¹, Shubao Shao,¹ Minglong Xu ¹ and Zijian Jing²

¹State Key Laboratory for Strength and Vibration of Mechanical Structures, School of Aerospace, Xi'an Jiaotong University, Xi'an 710049, China

²Key Laboratory of Beam Control, Institute of Optics and Electronics of Chinese Academy of Sciences, Chengdu 610209, China

Correspondence should be addressed to Minglong Xu; mlxu@xjtu.edu.cn

Received 20 February 2019; Accepted 11 April 2019; Published 1 July 2019

Academic Editor: Giovanni Berselli

Copyright © 2019 Ruijiang Xiao et al. This is an open access article distributed under the Creative Commons Attribution License, which permits unrestricted use, distribution, and reproduction in any medium, provided the original work is properly cited.

A novel hybrid-type $XY\theta_z$ micropositioning mechanism driven by piezoelectric actuators is proposed in this paper. With the purpose of realizing a large motion range and 3-DoF independent motion within a compact size, the mechanism is designed using a symmetric translational part and a rotational part that are linked serially. The translational part is based on a double-amplification mechanism incorporating a guidance mechanism for decoupling; the rotational part uses a nonuniform beam with an amplification mechanism to translate the linear output displacement of piezoelectric actuators into a large rotational angle around the Z axis. To precisely predict the output displacements and implement dimensional design, electromechanical models of the translational mechanism and rotational mechanism are established. According to the theoretical model, dimensional optimization is carried out to achieve large motion ranges within a compact size. A prototype of the proposed mechanism is fabricated according to the optimized results, and the performance of the mechanism is validated by experiment. The experimental results show that translational travel in X and Y directions of $204.2\ \mu\text{m}$ and $212.8\ \mu\text{m}$, respectively, and travel of $8.7\ \text{mrad}$ in the θ_z direction can be realized in a small size of $106\ \text{mm} \times 106\ \text{mm} \times 23\ \text{mm}$. And, the output coupling was evaluated to be below 3%, indicating an excellent decoupling performance.

1. Introduction

Three-degree-of-freedom (3-DoF) $XY\theta_z$ micropositioning mechanisms based on flexure hinges are widely applied in various fields; e.g., such mechanisms are used for atomic force microscopes, micromanipulation, scanning systems, high-precision image stabilization systems, and biomedical applications [1–7]. The mechanisms can improve the repeatability and reliability of scanning and image resolution of an optical-image stabilization system. Following the rapid development of optoelectronic technology and the expanding fields of implementation, it is necessary to correct the optical axis shift of space camera in real time and compensate image motion caused by low-frequency vibration via the design of servo mechanism in the optical path.

Therefore, the $XY\theta_z$ micropositioning mechanism with large travel, high displacement resolution, and compact structure that can be applied for the optical-image stabilization system is urgently required.

Generally, a piezoelectric actuator is commonly used in these micropositioning mechanisms because of its advantages of high positioning resolution, fast response, high stiffness, and no electromagnetic interference issues [8, 9]. However, the small deformation range of piezoelectric materials, which is merely about $1\ \mu\text{m}/\text{mm}$, restricts engineering applications. Existing piezo-actuated $XY\theta_z$ micropositioning mechanisms typically therefore have limited motion travel [10–12]. Hwang et al., for example, developed an in-plane $XY\theta_z$ positioning mechanism with dimensions of $240\ \text{mm} \times 240\ \text{mm} \times 25\ \text{mm}$ and translational and rotational motion ranges of $58\ \mu\text{m}$ and

1.05 mrad, respectively [11]. Zhu et al. presented a redundantly piezo-driven $XY\theta_z$ compliant mechanism with high dynamic characteristics but working ranges in X , Y , and θ_z directions of merely $12.42\ \mu\text{m}$, $24.82\ \mu\text{m}$, and $1.75\ \text{mrad}$, respectively [12]. To increase motion ranges, bridge-type amplification mechanisms are used for amplification of the deformation of piezoelectric materials because of their compact structure and high displacement amplifying ratio [13–17]. Although an existing $XY\theta_z$ micropositioning system having an amplification mechanism has larger working ranges, it employs larger stack-type actuators, which increase the system size [18]. Additionally, in the design of the above parallel-type $XY\theta_z$ mechanisms employing four or three actuators, the actuation of rotational motion shares the same piezoelectric stacks with the actuation of translational motion. This means that the strokes of rotation and translation cannot reach their expected maximum values simultaneously in reality [7, 18]. And also, the actuators of rotational part are often driven by high voltage for achieving large rotational angle, which limits practical application in the design of miniaturized instrument.

To overcome the aforementioned problems and satisfy the application in the optical-image stabilization system, a novel hybrid-type $XY\theta_z$ micropositioning mechanism featuring an enlarged workspace, compact size, and 3-DoF independent motion is proposed and developed in this study. The mechanism mainly comprises a translational part and rotational part, which are linked serially for kinematic decoupling. The parallel translational mechanism characterized by high precision and compactness uses a double-amplification mechanism incorporating a guidance mechanism for decoupling, aiming to realize large translational travel and guide the moving platform in the desired direction by preventing the platform from moving in a parasitic manner [19–21]. The rotational mechanism consists of a nonuniform beam and two piezoelectric actuators arranged in opposite directions. To translate the linear output displacement of the piezoelectric actuators into a larger output angle around the Z -axis at a lower voltage, a nonuniform beam with lever amplification is designed using flexure hinges. Generally, to estimate the output displacements of the $XY\theta_z$ micropositioning mechanism, electromechanical models of the translational mechanism and rotational mechanism are established employing a pseudo-rigid-body model and beam theory. Because of the finite stiffness of the piezo stack, the deformations affected by the input voltage and counterforce are simultaneously considered in this analysis, which improve the accuracy of the theoretical model. Using the established model, the mechanism is optimized to achieve larger motion ranges within a compact size. Finite element analysis (FEA) is then carried out to verify the output displacements and to investigate the dynamic performance of the mechanism. Finally, a prototype of the proposed micropositioning mechanism is fabricated according to the optimized parameters and the performance of the mechanism is experimentally validated.

2. Structure Design and Operating Principle

Figure 1 shows the structure of the proposed $XY\theta_z$ micropositioning mechanism, which mainly comprises a

translational part, rotational part, and the cruciform connecting structure illustrated in Figure 2(a). The parallel translational mechanism connected with the rotational part serially by the cruciform connecting structure employs a double-amplification mechanism including a rhombic piezoelectric actuator (RPA) and two levers that amplify the deformation of the piezo stack. On the basis of the right circular flexure hinges, the guidance mechanism is designed to deliver the platform high-resolution motion in desired (X and Y) directions and to restrict the platform in undesired directions. In the proposed mechanism, the rotational part consists of two piezoelectric actuators arranged in opposite directions, a nonuniform beam and a fixture. Figure 2(b) shows the design of the nonuniform beam, the two ends of which are fixed by flexure hinges. The beam consists of five segments. One rigid segment in the center works as an output port connected with the cruciform connecting structure by a groove and screw; two rigid arms are used to drive the output port; and two right circular flexure hinges are used to connect the above three rigid segments. Because of the symmetry of the translational part and the characteristic of hybrid-type design, independent motions of the platform along the X , Y , and θ_z directions can be achieved.

To actuate 3-DoF in-plane motion independently and achieve large motion ranges, the platform requires three pairs of piezoelectric actuators. The independent X -directional motion of the platform can be implemented by the coordinated work of piezoelectric actuators PZT1 and PZT3. Similarly, the Y -directional motion can be realized by actuating PZT2 and PZT4. When one pair of differential voltages is applied to the pair of piezoelectric actuators located on one axis (X or Y), the corresponding pair of RPAs applies forces and displacements to one end of the levers in a push-and-pull driving mode. In this mode, the RPAs produce displacements and forces in two opposing directions. In the first direction, as shown in Figure 3(a), the RPA produces a downward force or displacement, which is induced by an increase in the voltage input to the piezo stack, resulting in transverse elongation of the mechanism. In the second direction, the RPA produces an upward output, as shown in Figure 3(b), which is induced by a decrease in the input voltage, generating elastic recovery of the compliant mechanism. Therefore, when the voltage applied to the RPA of one axis (X or Y) is increased and the voltage applied to the RPA opposing that axis is decreased, the platform produces translational motion along that axis via the flexure guidance mechanism.

The independent θ_z -directional motion of the platform can be obtained by simultaneously driving PZT5 and PZT6. When a voltage pair is applied to the pair of oppositely located piezoelectric actuators in the rotational part, each piezoelectric actuator applies an actuation force on the rigid arm of the nonuniform beam in either the positive or negative Y direction (F and $-F$) through flexure hinges, generating a torque around the Z -axis, which imposes a tilt angle of the output port that allows the whole translational mechanism to generate θ_z -directional motion. Accordingly, 3-DoF independent in-plane motion of the platform can be achieved using the three pairs of piezoelectric actuators.

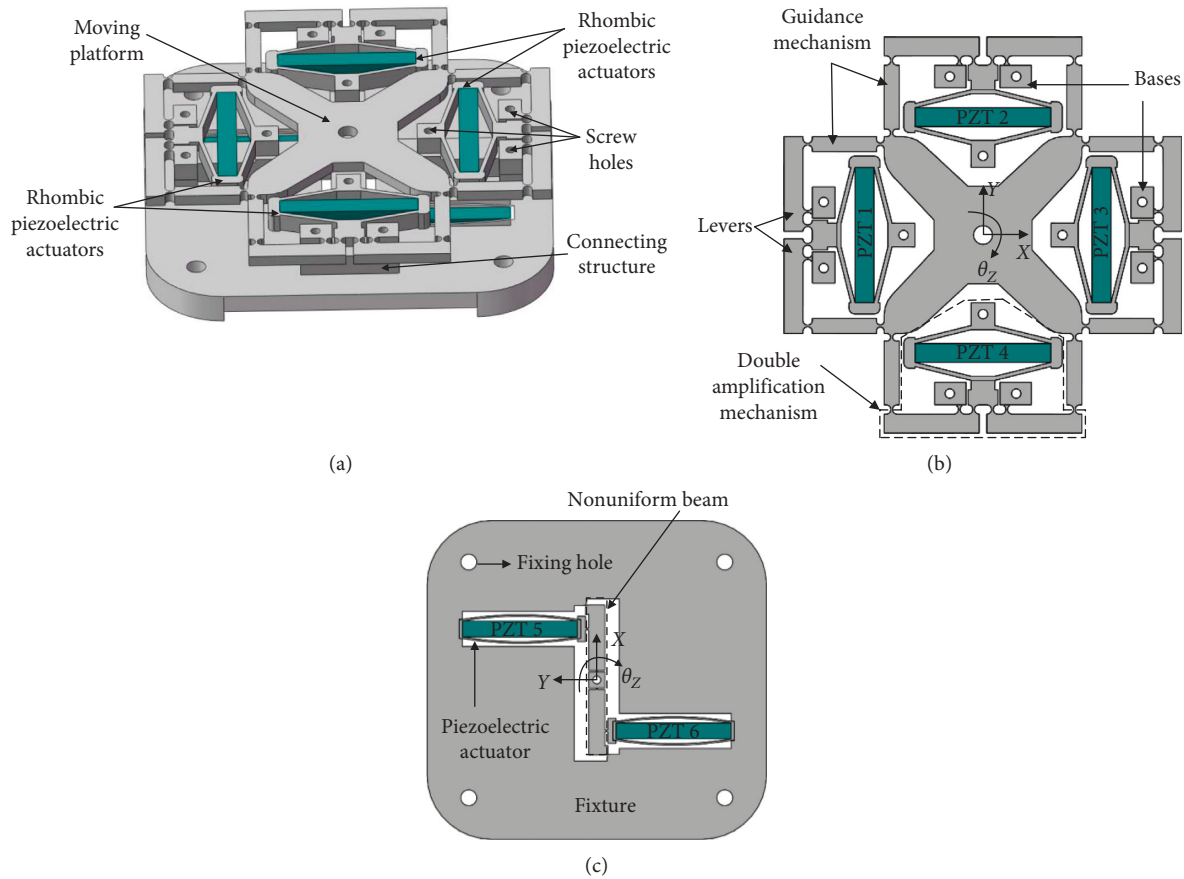


FIGURE 1: Model of the proposed $XY\theta_z$ micropositioning mechanism: (a) 3D model; (b) translational part; and (c) rotational part.

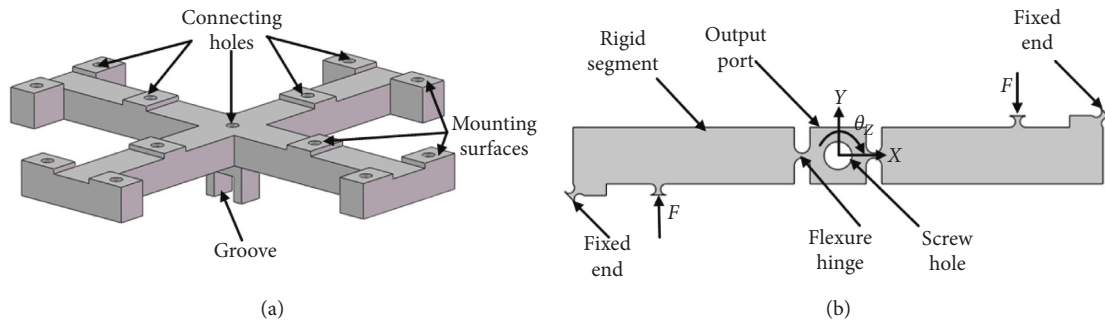


FIGURE 2: (a) Cruciform connecting structure and (b) nonuniform beam.

In the described micropositioning mechanism, the parallel-type translational motion part and the rotational motion part are decoupled and linked serially. The two parts are therefore modeled, respectively. The static analysis of the proposed mechanism is further discussed in Section 3.

3. Kinematic Analysis

3.1. Analysis of the Translational Mechanism. The translational mechanism can be abstracted as a serial mechanical network, as shown in Figure 4. To clarify the performance of the mechanism, it is necessary to establish an accurate theoretical model to comprehensively determine the

translational motion transmission from the piezo stacks to the platform. A governing equation of the RPA is therefore derived as a starting point for calculating the relationship of input-output static displacements and forces.

Because of the symmetry of the rhombic mechanism, we consider only a quarter of the structure as the study object. The mechanical model based on a pseudo-rigid-body model and Euler-Bernoulli beam theory is shown in Figure 5. In this analysis, the rhombic mechanism is considered to be constructed of rigid bodies interconnected by flexure arms in which the mechanism compliance is lumped. According to the energy principle, the input and output displacements of the structure can be expressed as

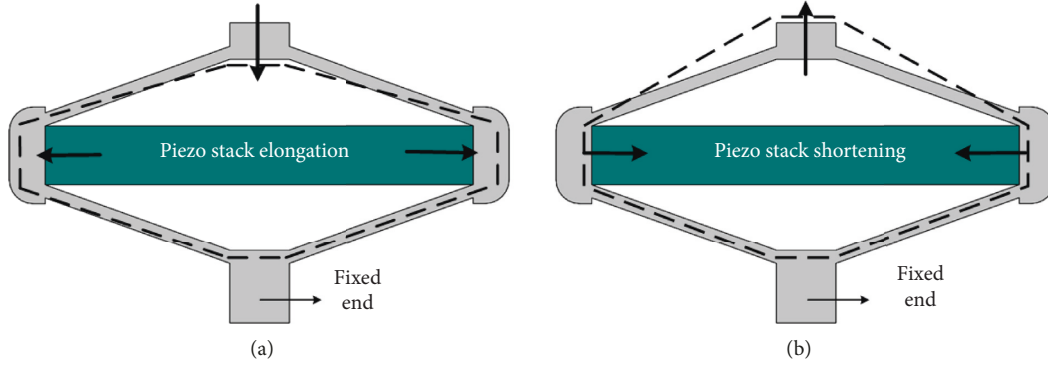


FIGURE 3: Schematics of the RPA: (a) pull driving mode; (b) push driving mode.

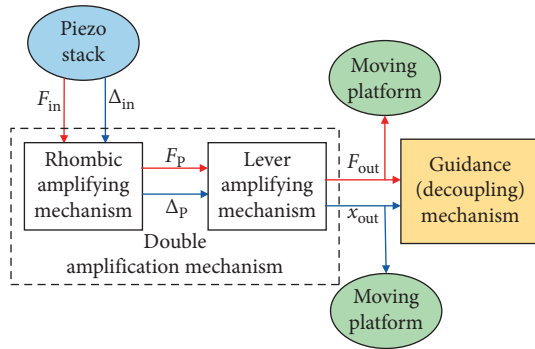


FIGURE 4: Schematic diagram of translational motion transmission.

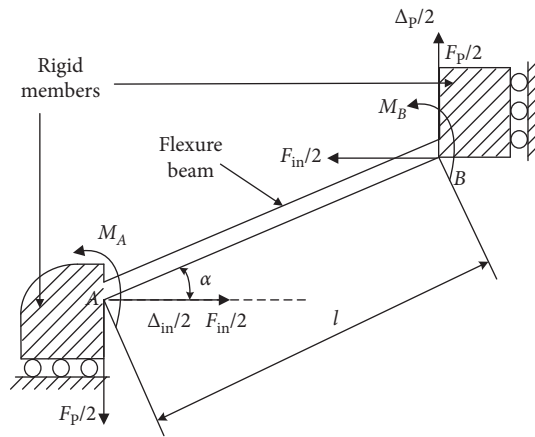


FIGURE 5: Model of a quarter of the rhombic mechanism.

$$\frac{\Delta_{in}}{2} = \int_0^l \frac{F_N(x)}{EA} \cdot 2 \frac{dF_N(x)}{dF_{in}} dx + \int_0^l \frac{M(x)}{EI} \cdot 2 \frac{dM(x)}{dF_{in}} dx, \quad (1)$$

$$\frac{\Delta_p}{2} = \int_0^l \frac{F_N(x)}{EA} \cdot 2 \frac{dF_N(x)}{dF_p} dx + \int_0^l \frac{M(x)}{EI} \cdot 2 \frac{dM(x)}{dF_p} dx. \quad (2)$$

Here, F_{in} is the driving force provided by the piezo stack, which produces input displacement Δ_{in} for the rhombic

mechanism, F_p is the output force, and Δ_p is the output displacement of the RPA; E is the elastic modulus; A and I are, respectively, the area and moment of inertia of the corresponding cross section of the beam; and $F_N(x)$ and $M(x)$ are, respectively, the axial tension and moment along the neutral axis. According to the static analysis shown in Figure 5, we have

$$\begin{cases} F_N(x) = \frac{1}{2} (F_p \sin \alpha - F_{in} \cos \alpha), \\ M(x) = \frac{1}{2} (F_p \cos \alpha + F_{in} \sin \alpha) \left(x - \frac{l}{2} \right). \end{cases} \quad (3)$$

By substituting equation (3) into equations (1) and (2), the relationship between input and output forces and thus the displacements can be obtained:

$$\begin{cases} F_{in} \cos \alpha - F_p \sin \alpha = \frac{EA}{l} (\Delta_{in} \cos \alpha - \Delta_p \sin \alpha), \\ F_{in} \sin \alpha + F_p \cos \alpha = \frac{2c}{l} (\Delta_{in} \sin \alpha + \Delta_p \cos \alpha). \end{cases} \quad (4)$$

Here,

$$c = \frac{6EI}{l^2}. \quad (5)$$

As mentioned above, the input displacement and force acting on the rhombic mechanism are provided by the piezo stack (P885.91, PI). When the hysteresis nonlinearity of the piezoelectric material is ignored, the linear deformation of the piezo stack can be written as

$$\delta = U_{in} C_V + \frac{1}{K_p} f_p, \quad (6)$$

where δ is the output displacement of the piezo stack, C_V is the piezoelectric constant and can be calculated as $C_V = n d_{33}$ (with n being the number of layers of the piezo stack), U_{in} is the change in the voltage applied to the piezo stack, K_p is the stiffness of the piezo stack, f_p is the external force imposed on the piezo stack, and $f_p = -F_{in}$. Thus,

$$\Delta_{in} = U_{in} C_V - \frac{1}{K_P} F_{in}. \quad (7)$$

Substituting (7) into (4), the governing equation of the RPA can be expressed in matrix form as

$$\begin{pmatrix} F_P \\ \Delta_P \end{pmatrix} = \frac{1}{\sin \alpha \cos \alpha (2c - EA)} \begin{bmatrix} 2c \cos^2 \alpha + EA \sin^2 \alpha + \frac{2EAc}{K_P l} & \frac{2EAc}{l} \\ l + \frac{1}{K_P} (EA \cos^2 \alpha + 2c \sin^2 \alpha) & EA \cos^2 \alpha + 2c \sin^2 \alpha \end{bmatrix} \begin{pmatrix} F_{in} \\ C_V U_{in} \end{pmatrix} \quad (8)$$

$$= \begin{bmatrix} f_{11} & f_{12} \\ f_{21} & f_{22} \end{bmatrix} \begin{pmatrix} F_{in} \\ C_V U_{in} \end{pmatrix}.$$

To further characterize the output displacement of the double-amplification mechanism, the mechanical model of the lever mechanism is shown in Figure 6. The right circular flexure hinges sharing the same geometry configuration are simplified as rotational springs attached to the lever. Each flexure hinge therefore imposes an angular moment on the lever:

$$M_k = K_{r1} \theta_k, \quad k = C, O, D, \quad (9)$$

where θ_k is the rotational angle of the hinges and equals the tilt angle of the rigid lever. θ_k can be expressed as $\theta_k = \Delta P / L_2$ owing to the small value of θ_k . K_{r1} is the rotation stiffness of right circular flexure hinge 1, which can be calculated using the equations presented by Zhu et al. [22]. The force equilibrium equation and geometrical equation of the rigid lever are then established:

$$\begin{cases} M_C + M_O + M_D + F_{Cy} L_1 - F_{Dy} L_2 = 0, \\ \Delta_{out} = \frac{L_1}{L_2} \Delta_P, \end{cases} \quad (10)$$

where F_{Cy} and F_{Dy} are vertical forces of nodes C and D, and $F_{Dy} = -F_P / 2$.

In the analysis of the parallel configuration, the reaction of the guidance mechanism can be considered equivalent to an elastic load with port stiffness of K_{load} . According to Newton's third law of motion, the output force of the double-amplification mechanism is then

$$F_{out} = -F_{Cy} = -\frac{K_{load} x_{out}}{4}. \quad (11)$$

The mechanical model of the guidance mechanism with four rods is shown in Figure 7. The equivalent stiffness K_{load} can be expressed as

$$K_{load} = 4k_x, \quad (12)$$

where k_x is the stiffness in the x direction of each guidance rod and be calculated as

$$k_x = \frac{K_{r1} + K_{r2}}{L_3^2}, \quad (13)$$

with K_{r2} being the rotation stiffness of right circular flexure hinge 2.

Owing to the symmetry of the translational mechanism, the output displacements along X and Y axes are equal. The electromechanical model of the translational mechanism, which relates the output displacement of the translational mechanism to the voltage applied to the piezo stack, can therefore be obtained from equations (8)–(11) as

$$x_{out} = \frac{2L_1 L_2}{12K_{r1} + K_{load} L_1^2} \left[\frac{f_{22} (12K_{r1} + K_{load} L_1^2) + 2f_{12} L_2^2}{f_{21} (12K_{r1} + K_{load} L_1^2) + 2f_{11} L_2^2} - f_{12} \right] \cdot C_V U_{in}. \quad (14)$$

3.2. Analysis of the Rotational Mechanism. In this subsection, to accurately establish a theoretical model of the rotational mechanism, the nonuniform beam is modeled using the stiffness equation of the flexible segments. It is assumed that the compliance of the rotational part is lumped in the flexure hinges and the flexible segments of the beam. The modeling of the mechanism therefore begins with the analysis of the flexure connectors.

The flexible segment, namely, the right circular hinge, is used to connect the rigid segments and to deliver high-resolution motion to the output port. Figure 8 shows the degrees of freedom of the two nodes and the nodal loads of a right circular hinge in the coordinate system originating at node i . The stiffness equation of the right circular hinge can be referred to the literature [22].

In the nonuniform beam, the other flexure joints between rigid bodies also employ right circular flexure hinges to fix the two ends of the beam and connect the beam with two piezoelectric actuators. These flexure hinges have the same geometrical configuration. A mechanical model of the beam is established to characterize the static response of the structure. The right circular flexure hinges are simplified as rotational springs. The flexure hinges then impose an angular moment M_i ($i = A1, B1, C1, D1$) on the rigid beams, as shown in Figure 9. We thus have

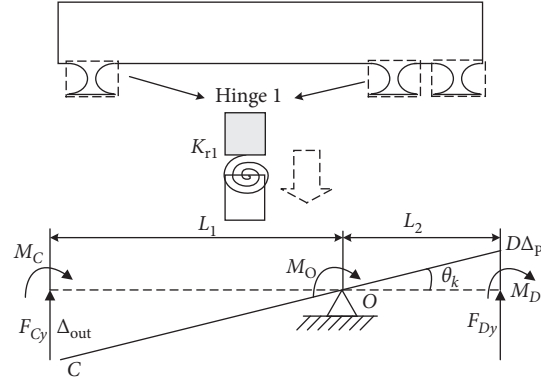


FIGURE 6: Mechanical model of the lever mechanism.

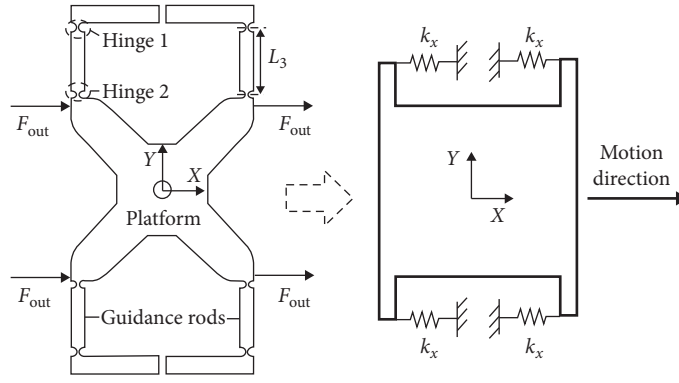


FIGURE 7: Mechanical model of the guidance mechanism.

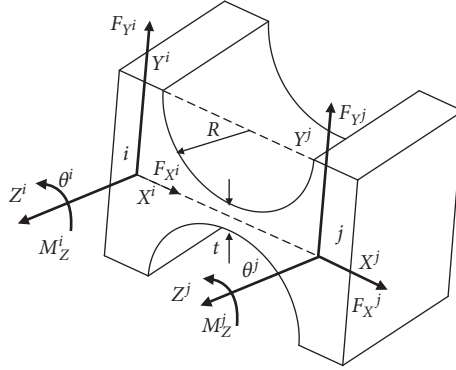


FIGURE 8: Schematic of the right circular flexure hinge.

$$M_i = K_{r3}\theta_i, \quad i = A1, B1, C1, D1, \quad (15)$$

where θ_i is the rotational angle of the hinges and equals the tilt angle of the rigid arms. K_{r3} is the rotation stiffness of flexure hinge 3.

The force equilibrium equations of the beam can then be derived:

$$\begin{cases} F_{A1} + F_{C1} = F_{B1} + F_{D1}, \\ M_{A1} + M_{B1} + M_{C1} + M_{D1} - F_{B1}x + F_{C1}(L-x) = F_{D1}L, \end{cases} \quad (16)$$

where F_{B1} and F_{C1} are the actuation forces provided by two piezoelectric actuators and $F_{B1} = F_{C1} = F$.

From equation (16), the nodal forces of the right circular flexure hinge used to construct a flexible segment at point E can be expressed as

$$\begin{cases} F_E = \frac{1}{L}(2Fx - 4K_{r3}\theta_i), \\ M_E = \left(1 - \frac{2l_a}{L}\right)(Fx - 2K_{r3}\theta_i). \end{cases} \quad (17)$$

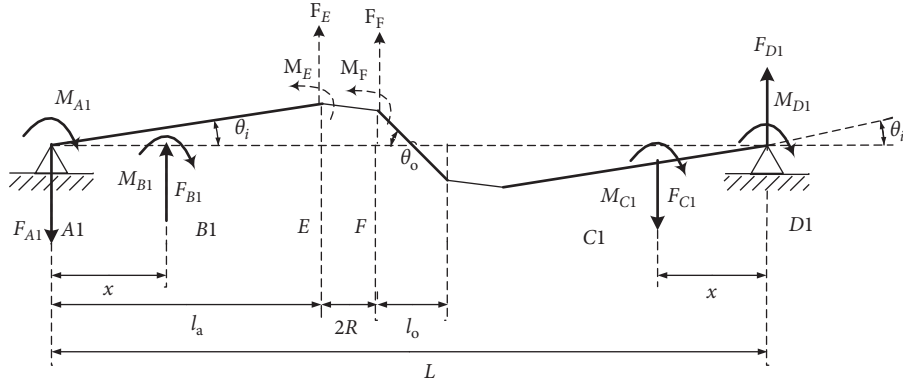


FIGURE 9: Simplified model of the nonuniform beam.

The axial loads are ignored in this analysis owing to the small deformation of the beam. The stiffness equation of the right circular flexure hinge can therefore be derived to characterize the deflection of the beam:

$$F_R = K_R X_R, \quad (18)$$

where

$$F_R = [F_E \ M_E \ F_F \ M_F]^T,$$

$$X_R = [\Delta_{yE} \ \Delta_{\theta E} \ \Delta_{yF} \ \Delta_{\theta F}]^T = \left[\theta_i l_a \ \theta_i \ \theta_o \frac{l_o}{2} \ -\theta_o \right]^T,$$

$$K_R = \frac{1}{C_1 C_3 - C_2^2} \begin{bmatrix} C_1 & C_2 & -C_1 & C_2 \\ C_2 & C_3 & -C_2 & 2RC_2 - C_3 \\ -C_1 & -C_2 & C_1 & -C_2 \\ C_2 & 2RC_2 - C_3 & -C_2 & C_3 \end{bmatrix}, \quad (19)$$

with C_m ($m = 1 - 4$) denoting the compliance, which refers to the displacements produced by the corresponding applied forces, and R being the cutting radius.

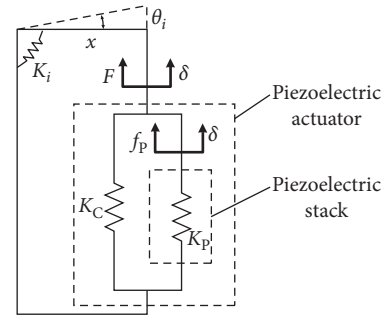


FIGURE 10: Model of the piezoelectric actuator.

Then, from (17) and (18), the defined equivalent stiffnesses K_o and K_i can be obtained:

$$\begin{cases} K_o = \frac{Fx}{\theta_o} = \frac{[pL(C_1 l_a + C_2) + 4K_{r3}]f - pL(C_1(l_o/2) + C_2)}{2}, \\ K_i = \frac{Fx}{\theta_i} = \frac{K_o}{f}, \end{cases} \quad (20)$$

where

$$p = \frac{1}{C_1 C_3 - C_2^2}, \quad (21)$$

$$f = \frac{C_2 l_a + 2(2RC_2 - C_3) - (L - 2l_a)(C_1(l_o/2) + C_2)}{2[C_2 l_a + C_3 + (2/p)(1 - (2l_a/L))K_{r3}] - (L - 2l_a)(C_1 l_a + C_2 + (4K_{r3}/pL))}.$$

According to (20), the output angle θ_o depends on the moment $M = Fx$ that is derived from the actuation force generated by one piezoelectric actuator. It is therefore necessary to obtain the force F of the piezoelectric actuator that consists of a preloading mechanism and a piezo stack. A simplified model of the piezoelectric actuator is thus built as shown in Figure 10. In this model, the piezo stack is equivalent to a source of displacement connecting in series with a spring, which has stiffness K_p . The preloading

mechanism, which has stiffness K_c , is incorporated with the piezo stack to output the actuation force F . The force equilibrium equation can be established according to the deformation equation of the piezo stack given as equation (6):

$$F = (C_V U_{in} - \delta)K_p - \delta K_c, \quad (22)$$

where δ is given by $\delta = x\theta_i$ owing to the small value of θ_i . By substituting equation (22) into (20), the electromechanical

model of the rotational part, which relates the output angle around the Z axis of the mechanism to the voltage applied to the piezo stack, is obtained:

$$\theta_o = \frac{Fx}{K_o} = \frac{xK_p C_V}{f[x^2(K_p + K_c) + K_i]} U_{in}. \quad (23)$$

4. Dimensional Optimization

According to the above theoretical analysis, it is obvious that the dimensions are critical to the actuation performance of the $XY\theta_z$ micropositioning mechanism. Hence, to confirm the dimensions of the X/Y -directional part and θ_z -directional part, design optimization is performed in this section with the goal of achieving large motion travel within a compact size.

According to (14) and (23), the output displacements of the mechanism rely on parameters of the geometric configuration, the performance of the piezoelectric actuators, machining feasibility, and material properties. In this optimization analysis, aluminum alloy AL7075-T6 is used because it has a high ratio of the yield strength to Young's modulus. To reduce the rotation stiffness and increase the rotation precision of the right circular flexure hinges, the hinge thickness and cutting radius should be designed as small as possible. However, the minimum of the two parameters has to be larger than 0.3 mm to avoid the melting of the material during wire electro-discharge machining. In addition, to achieve a low-voltage design in specific cases, the range of the operating voltage in the rotational part is set from 0 to 50 V. All these fixed parameters are given in Table 1.

The output displacements in the X/Y direction and θ_z direction are therefore functions formulated by equations (14) and (23), respectively, in terms of the remaining design parameters. Then, equations of the objective functions are determined as follows:

$$\begin{aligned} \text{Maximum } x_{out} &= f_1(\alpha, w, L_1), \\ \text{Maximum } \theta_o &= f_2(l_a, l_o, R, x). \end{aligned} \quad (24)$$

The constraints are described as follows:

- (1) To satisfy several specifications, these design parameters are constrained. To achieve a compact size, the following geometric constraints are imposed for the optimal design:

$$\begin{cases} L_1 + L_2 = 21.8, & 10 \leq L_1 \leq 20, \\ 5 \leq \alpha \leq 40, & 1 \leq w \leq 4, \\ 2l_a + 4R + l_o \leq 44.2, & 6 \leq x \leq 21, \\ 5 \leq l_o < 48, & 0.3 \leq R \leq 3. \end{cases} \quad (25)$$

- (2) In order to guarantee design reliability, the following maximum stress at each outer surface of the thinnest part of the flexure hinge needs to be treated [19]:

TABLE 1: Fixed parameters of the mechanism.

Piezoelectric actuator (P885.91, Physik Instrumente, Germany)	
Stiffness of the piezo stack	25 N/ μ m
Stiffness of the preloading mechanism	5.89 N/ μ m
Size of piezo stack	5 mm \times 5 mm \times 36 mm
Operating voltage	-20 V-120 V
Piezoelectric constant	0.316 μ m/V
Material (Al 7075)	
Elastic modulus	72 GPa
Shear modulus	27 GPa
Density	2750 kg/m ³
Yield strength	500 MPa
Right circular flexure hinge 1	
Hinge thickness, t_1	0.4 mm
Cutting radius, R_1	1.2 mm
Right circular flexure hinge 2	
Hinge thickness, t_2	0.5 mm
Cutting radius, R_2	1.0 mm
Right circular flexure hinge 3	
Hinge thickness, t_3	0.4 mm
Cutting radius, R_3	0.5 mm

$$\sigma_{max} = \frac{E(1 + \beta)^{9/20}}{\beta^2 f(\beta)} \theta \leq [\sigma] = \frac{\sigma_y}{n}, \quad (26)$$

where $\beta = t/R$, θ is an angular displacement, σ_y is the yield stress of the material, and n is the safety factor.

The optimization process can be carried out in MATLAB software to investigate how the maximum output displacement depends on each parameter in a given range; for an arbitrary value of a parameter, there is a corresponding maximum of the output displacement in the parameter space formed by the given domain of the remaining parameters. The optimization results are shown in Figures 11–13.

Figures 11(a) and 11(b) show how the translational displacement changes with beam angle α , thickness w , and length L_1 . It can be seen from Figure 11(a) that when the angle α is constant, the output displacement increases as the thickness w decreases. Thus, the thickness w of the beam should be the minimum value in its range. Angle α and length L_1 reach their respective thresholds when the translational displacement is a maximum, and when α or L_1 increases continuously, the maximum translational displacement decreases. Figure 12 shows the dependence of the maximum translational travel on α and L_1 when thickness w is taken as constant as discussed above. The constraint for α and L_1 is shown as a plane in this 3D plot. It is seen that the translational travel has a maximum value. The thresholds of α and L_1 at the maximum displacement can therefore be calculated as

$$\begin{cases} \frac{\partial f_1(\alpha, L_1)}{\partial L_1} = 0, \\ \frac{\partial f_1(\alpha, L_1)}{\partial \alpha} = 0. \end{cases} \quad (27)$$

Figure 13(a)–13(d) shows the dependence of the maximum angle travel θ_z on the design parameters of the

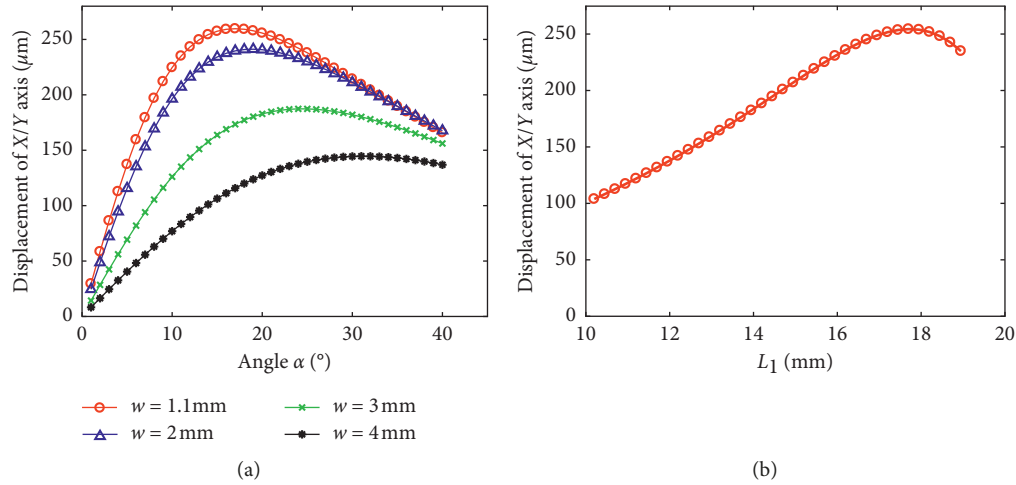


FIGURE 11: Dependence of the maximum translational displacement on the designed parameters.

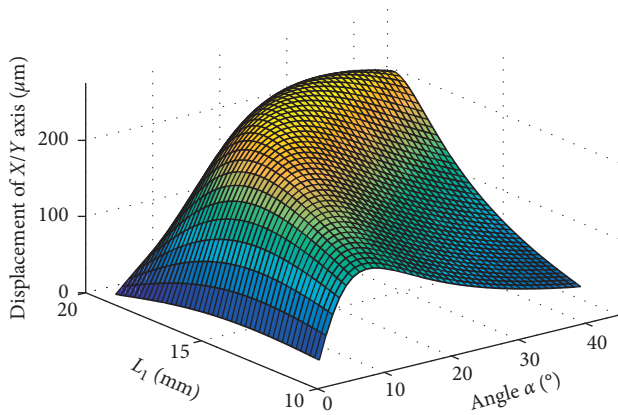


FIGURE 12: Maximum translational displacement plot in terms of L_1 and α .

θ_z -directional part. These plots clearly show that l_a should take a maximum value while l_o , R , and x should take minimum values in their ranges.

The optimization results of the design parameters of the X/Y-directional part and θ_z -directional part are summarized in Table 2.

5. FEA

In this section, FEA of the $XY\theta_z$ micromechanism is carried out using ANSYS software according to the optimized parameters. The 3D model is generated by Solidworks and imported to ANSYS. A multiphysics analysis is then conducted to estimate the performance of the mechanism.

To begin with, a static analysis via FEA numerical simulation is conducted to validate the output displacements of the mechanism. In order to calculate the output displacements accurately, piezoelectric stacks are defined as piezoelectric bodies in ANSYS software. And, voltage boundary conditions are exerted to two surfaces of corresponding piezoelectric stack. The results are shown in Figure 14. Figure 14(a) shows the motion of the platform along the positive X-axis with a driving voltage of 70 V. And, the

maximum bidirectional translational travel can be obtained; the output displacement in the X/Y direction is $240.0 \mu\text{m}$. In addition, when the platform is driven in the X direction, the output displacement in the Y direction is almost zero, which shows excellent output decoupling performance of the micropositioning mechanism. Therefore, when the two pairs of PZTs in the translational part are given the same voltages simultaneously, the platform has motion in a direction 45 degrees to the X-axis as seen in Figure 14(b). The motion in the θ_z direction is shown in Figure 14(c), and the rotational angle around the Z-axis is determined as 10.0 mrad . The maximum stress at maximum deformation is 345.9 MPa and occurs in the flexure hinge. It is lower than the yield stress of the material which is 500 MPa . Meantime, the rotational motion of the whole structure around Z-axis is shown in Figure 14(d). It can be seen that the torsional motion does not cause the translational displacement in X/Y direction because of the excellent decoupling characteristics of the mechanism.

The results of theoretical analysis and FEA are compared in Table 3. The corresponding relative errors of output displacements in the X/Y direction and θ_z direction are about 8.2% and 13.0%, respectively. The output displacements obtained from FEA are smaller than the theoretical values. This is mainly due to the rigid levers and rigid arms having elastic deformation in the FEA.

Moreover, the modal analysis of the mechanism with consideration of piezoelectric actuators is also carried out through FEA to investigate the dynamic performance. The modal analysis results in Figure 15(a)–15(c) show that natural frequencies along the θ_z , Y, and X directions are about 105, 505, and 518 Hz.

A prototype of the $XY\theta_z$ micropositioning mechanism was fabricated according to the results of optimization. The translational part and rotational part were monolithically machined from AL-7075 using wire electro-discharge machining technology for high precision. As shown in Figure 16, the overall dimensions of the

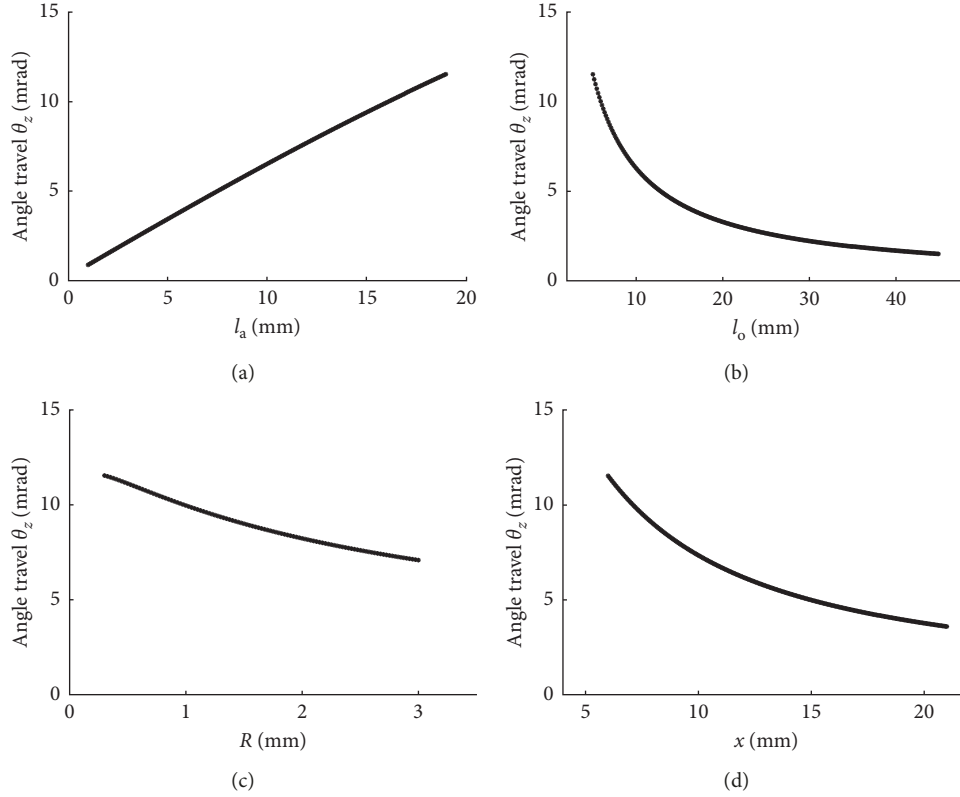


FIGURE 13: Dependence of the angle travel θ_z on the design parameters: (a) l_a ; (b) l_o ; (c) R ; (d) x .

TABLE 2: Optimization parameters and results.

Parameters	X/Y-directional part			θ_z -directional part			
	w	α	L_1	l_a	l_o	R	x
Parameter limit							
Lower	1	5	10	0	5	0.3	6
Upper	4	40	20	19	48	3	21
Optimization results	1	17	17.8	19	5	0.3	6
Unit	mm	deg	mm	mm	mm	mm	mm

prototype were $106 \text{ mm} \times 106 \text{ mm} \times 23 \text{ mm}$. Three pairs of piezo stacks (P885.91, PI) were used to drive the platform.

6. Experiment

The basic characteristics of the mechanism are experimentally investigated in this section. The principle experimental components are pictured in Figure 17. A LabVIEW system (LabVIEW 8.5 with NI PXI-1050) was used to generate the driving signals that were sent to the power amplifier (PA-12D developed at Xi'an Jiaotong University) and to acquire the signal of output displacements from the laser sensor. To measure the output displacements, two pairs of differential voltages were applied to the two pairs of piezoelectric actuators located in the translational part and one pair of the same voltage was applied to the actuators located in the rotational part. Figure 18 shows the relationship of output displacements in X , Y , and θ_z directions

with input voltages. The input voltage of each axis is described by the one input voltage of the voltage pair to the corresponding axis. To achieve a low-voltage design in specific cases and guarantee the security of the structure, the range of the operating voltage in the rotational part is set from 0 to 50 V.

Figure 18(a) shows that the output displacement along the X -axis reached $204.2 \mu\text{m}$, which is slightly shorter than the output displacement along the Y -axis ($212.8 \mu\text{m}$) for a voltage of 120 V. These errors seem to originate from the difference in piezo stacks, machining errors, and installation errors of the mechanical structures. Figure 18(b) shows that the output angle around Z -axis reached 8.7 mrad with a driving voltage of 50 V.

Owing to the design of the guidance mechanism and the symmetrical design of the translational part, there is no coupling displacement between the X -axis and Y -axis in theory. However, it is virtually impossible to achieve absolute symmetry of the mechanism owing to the machining and installation errors of piezoelectric actuators. Therefore, the coupling displacement of the two axes was also tested by using the sinusoidal input signal in this work. Figure 19 shows the output displacements when only the X -axis was actuated. It is seen that the maximum coupling error along the Y -axis was about 2.5%. Similarly, when only the Y -axis was actuated, the corresponding maximum coupling error along the X -axis was about 2.9%.

Figure 20 compares the experimental results with the results of FEA. There are two curves for each direction of the

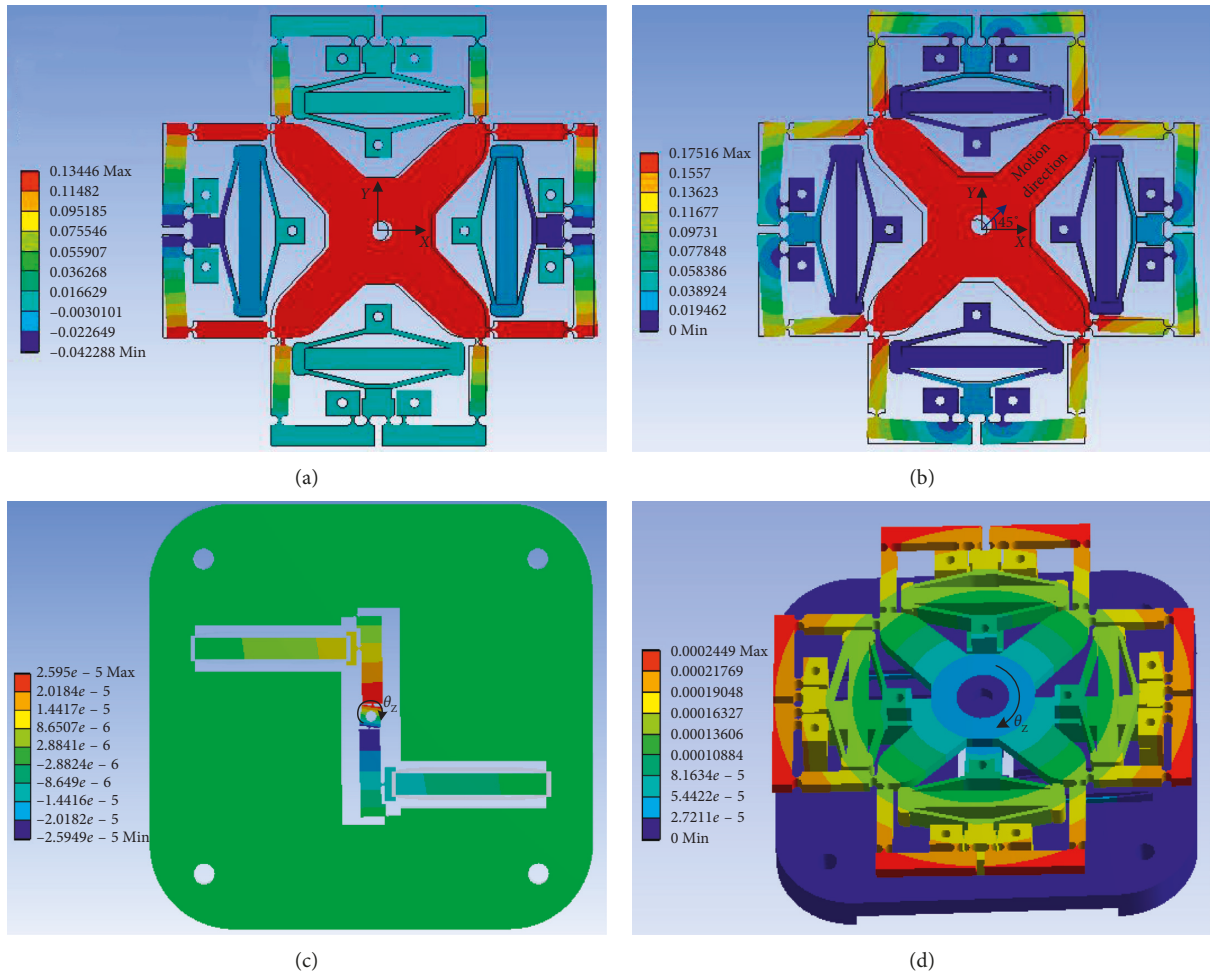


FIGURE 14: Results of static analysis: (a) motion along the positive X -axis; (b) motion in a direction 45 degrees to the X -axis; (c) motion of rotational part; (d) motion of the entire structure in the θ_z direction.

TABLE 3: Comparison of outputs obtained employing the theoretical model and FEA.

	X/Y (μm)	θ_z (mrad)
Theoretical modal	259.7	11.3
Finite element analysis	240.0	10.0
Error (%)	8.2	13.0

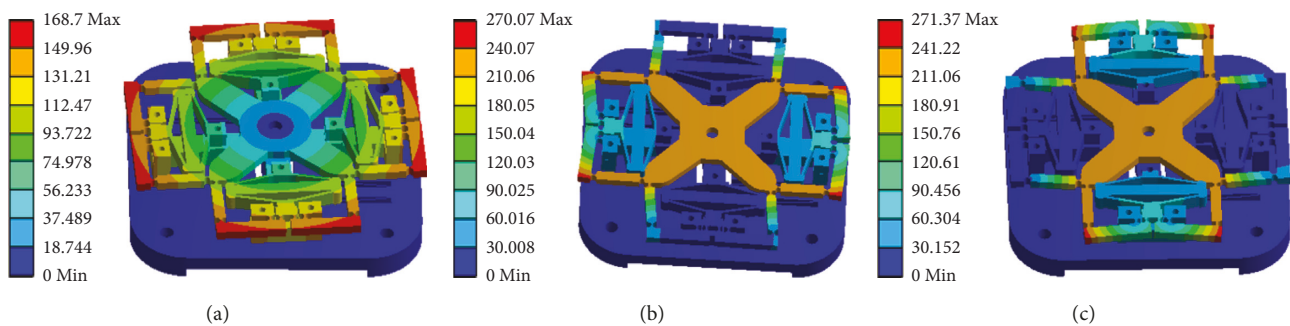


FIGURE 15: Modal shapes of the structure in (a) θ_z direction, (b) Y direction, and (c) X direction.

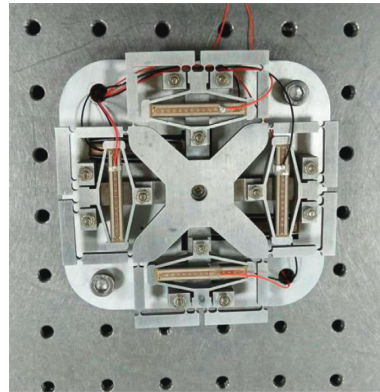


FIGURE 16: Prototype of the $XY\theta_z$ micropositioning mechanism.

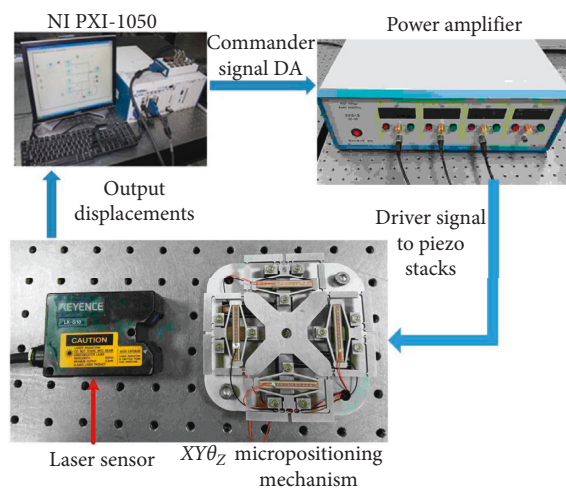


FIGURE 17: Principle and experimental setup of the mechanism.

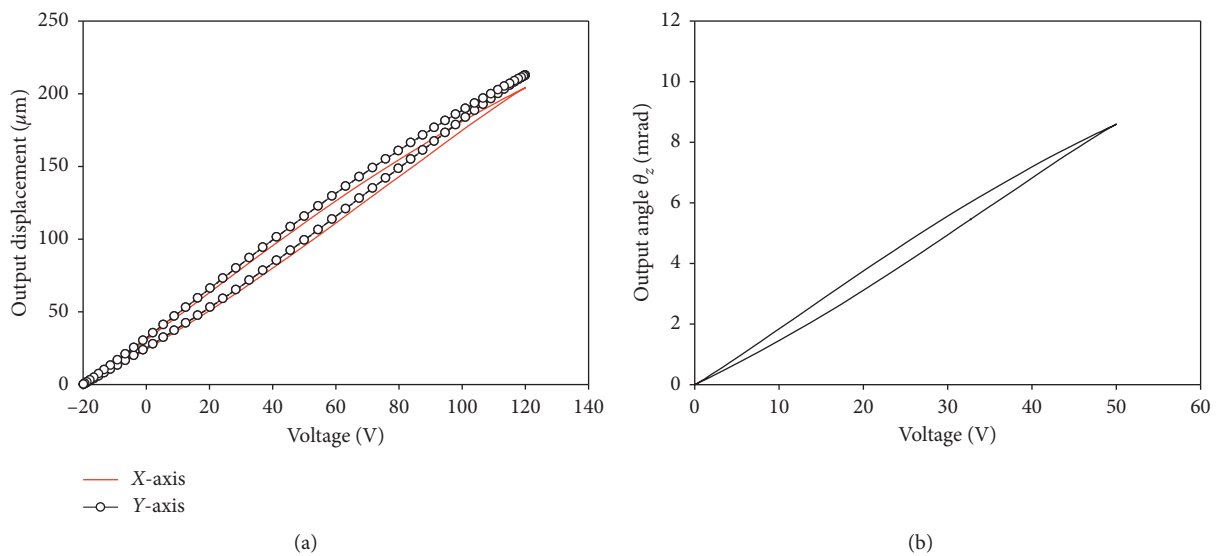


FIGURE 18: Tested output displacements in (a) X and Y directions and (b) θ_z direction.

experimental result because of the hysteresis of piezo stacks. The experimental results indicate that the actual translational travel and rotational angle around the Z axis were

smaller than the results obtained using the finite element model, and the corresponding maximum relative differences (i.e., errors) between the experimental results and FEA were

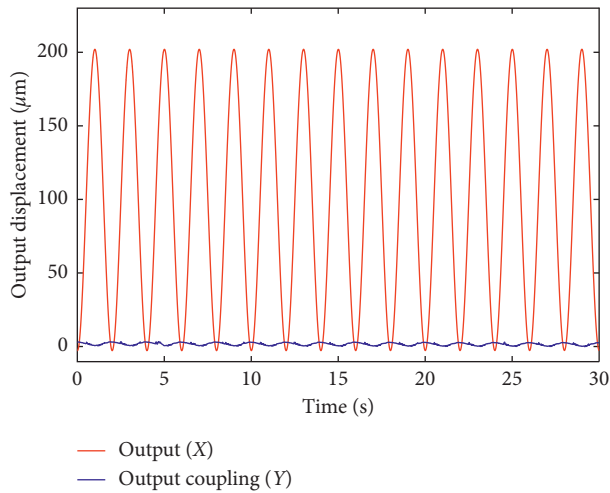


FIGURE 19: Coupling error of the translational part.

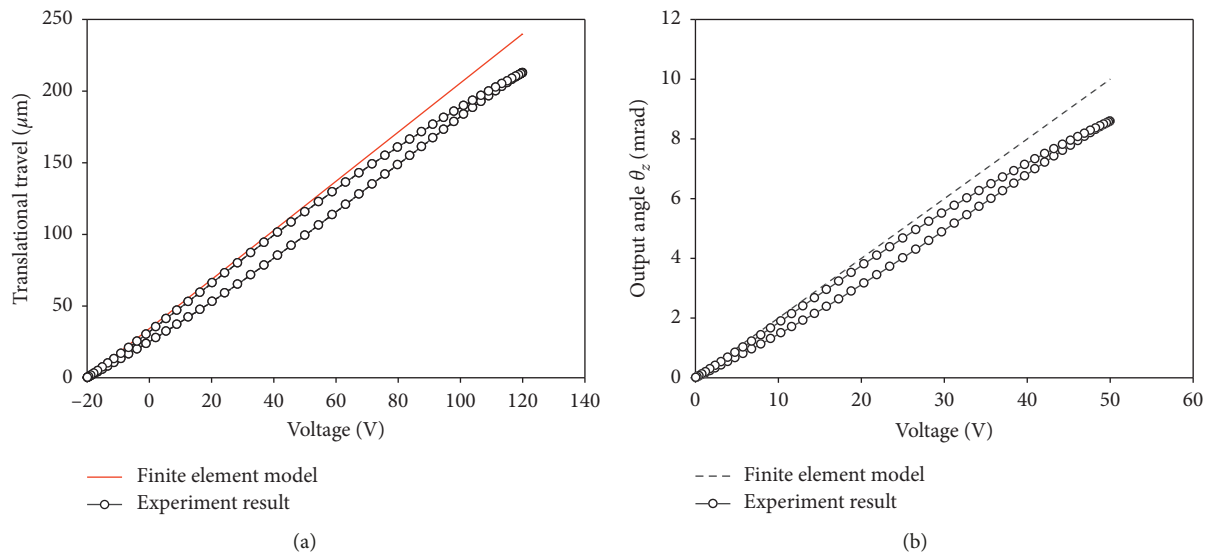


FIGURE 20: Comparison of the finite element model and experiment results: (a) translational travel; (b) output angle around the Z-axis.

about 12.7% and 14.9%, respectively. These errors mainly originated from machining errors and installation errors of the mechanical structures.

To determine the first natural frequency of the platform, the frequency response was measured. Sweeping sinusoidal signals were used to excite the PZTs in θ_z direction, and frequency response signal was measured by using laser sensor. Figure 21 shows that the first natural frequency is 87.8 Hz, which is slightly smaller than the FEA result. The deviation may be due to machining error and installation error of the structure. The additional mass caused by the mounting screws and the wires of the piezoelectric stacks can also reduce the natural frequency of the actual structure.

In addition, the motion resolution is tested. As can be seen in Figure 22, the minimum resolutions are clearly resolved from the multistep response experiment, which are 52 nm in the X/Y-axis and 9 μrad in the θ_z -axis, respectively.

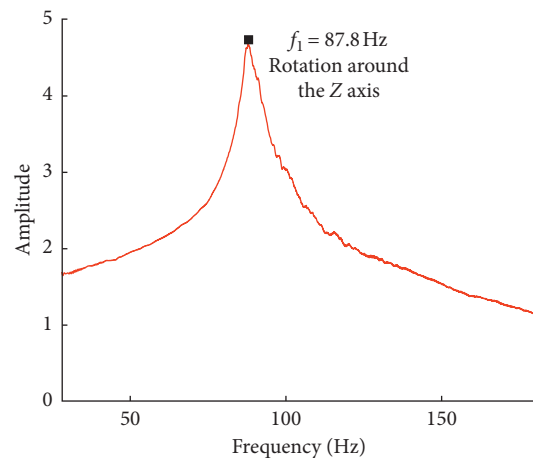


FIGURE 21: Tested first natural frequency of the mechanism.

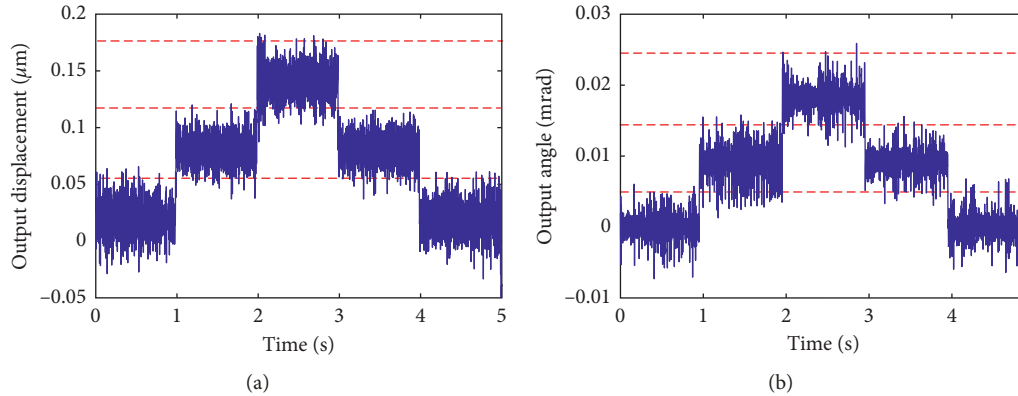


FIGURE 22: Multistep response for the resolution test: (a) X/Y-axis; (b) θ_z -axis.

In this test, the movement of the platform is measured by KEYENCE laser displacement sensor. The resolution of laser sensor is lower than the capacity position sensor. If the resolution of the displacement sensor can be improved, a higher resolution of the developed structure can be achieved.

7. Conclusions

This paper presents the design, modeling, optimization, and experimental testing of a novel piezo-actuated $XY\theta_z$ micropositioning mechanism featuring large travel, compact size, and 3-DoF independent motion. This mechanism consists of a translational motion part and a rotational motion part, which are linked serially. To achieve large motion ranges, electromechanical models of the translational mechanism and rotational mechanism were established to describe the relationship between the input voltages and the output displacements. The mechanism was then optimized using the theoretical model, realizing large output displacements within a compact size. On the basis of optimized parameters, the FEA results of the mechanism confirmed that the parallel translational part was well decoupled. Finally, a prototype of the mechanism with dimensions of $106\text{ mm} \times 106\text{ mm} \times 23\text{ mm}$ was fabricated. Experimental results show that translational travel in X and Y directions was, respectively, 204.2 and $212.8\text{ }\mu\text{m}$, while travel of 8.7 mrad in the θ_z direction could be realized. And, the minimum resolutions are 52 nm in the X/Y-axis and $9\text{ }\mu\text{rad}$ in the θ_z -axis. In addition, the output coupling was evaluated to be below 3%, indicating an excellent decoupling performance. These results show that the developed $XY\theta_z$ micropositioning mechanism can be used in several industrial applications that require large motion ranges within small spaces, especially the optical image stabilization system. The testing of closed-loop control of the micropositioning mechanism will be presented in future work.

Data Availability

The data used to support the findings of this study are available from the corresponding author upon request.

Conflicts of Interest

The authors declare that there are no conflicts of interest regarding the publication of this paper.

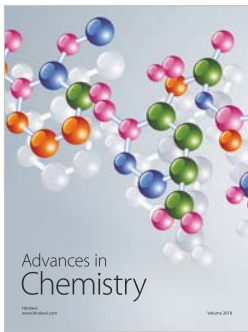
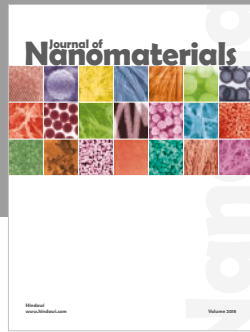
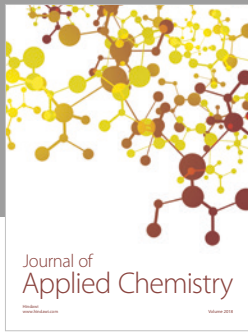
Acknowledgments

This work was supported by the National Natural Science Foundation of China (Grant Nos. 11672352 and 11872050).

References

- [1] D. Mukhopadhyay, J. Dong, E. Pengwang, and P. Ferreira, "A SOI-MEMS-based 3-DOF planar parallel-kinematics nanopositioning stage," *Sensors and Actuators A: Physical*, vol. 147, no. 1, pp. 340–351, 2008.
- [2] U. Bhagat, B. Shirinzadeh, L. Clark et al., "Design and analysis of a novel flexure-based 3-DOF mechanism," *Mechanism and Machine Theory*, vol. 74, pp. 173–187, 2014.
- [3] R. Wang and X. Zhang, "A planar 3-DOF nanopositioning platform with large magnification," *Precision Engineering*, vol. 46, pp. 221–231, 2016.
- [4] H. Y. Kim, D. H. Ahn, and D. G. Gweon, "Development of a novel 3-degrees of freedom flexure based positioning system," *Review of Scientific Instruments*, vol. 83, no. 5, article 055114, p. 11, 2012.
- [5] Y. Tian, B. Shirinzadeh, and D. Zhang, "Design and dynamics of a 3-DOF flexure-based parallel mechanism for micro/nano manipulation," *Microelectronic Engineering*, vol. 87, no. 2, pp. 230–241, 2010.
- [6] D. Hwang, J. Byun, J. Jeong, and M. G. Lee, "Robust design and performance verification of an in-plane $XY\theta$ micropositioning stage," *IEEE Transactions on Nanotechnology*, vol. 10, no. 6, pp. 1412–1423, 2011.
- [7] J. Park, H. Lee, H. Kim, H. Kim, and D. Gweon, "Note: development of a compact aperture-type $XY\theta_z$ positioning stage," *Review of Scientific Instruments*, vol. 87, no. 3, article 036112, p. 3, 2016.
- [8] Z. Jing, M. Xu, and B. Feng, "Modeling and optimization of a novel two-axis mirror-scanning mechanism driven by piezoelectric actuators," *Smart Materials and Structures*, vol. 24, no. 2, article 025002, p. 12, 2015.
- [9] H. Yang and W. Zhu, "A modified comprehensive model for piezoelectric stack actuators and corresponding parameter

- identification method,” *Advances in Materials Science and Engineering*, vol. 2015, Article ID 215836, 11 pages, 2015.
- [10] K. Cai, Y. Tian, F. Wang, D. Zhang, and B. Shirinzadeh, “Development of a piezo-driven 3-DOF stage with T-shape flexible hinge mechanism,” *Robotics and Computer-Integrated Manufacturing*, vol. 37, pp. 125–138, 2016.
- [11] D. Hwang, M. G. Lee, and J. Jeong, “Note: “Design of a novel ultraprecision in-plane $XY\theta$ positioning stage,” *Review of Scientific Instruments*, vol. 82, no. 2, article 026102, p. 3, 2011.
- [12] W. L. Zhu, Z. Zhu, S. To, Q. Liu, B. F. Ju, and X. Zhou, “Redundantly piezo-actuated $XY\theta_z$ compliant mechanism for nano-positioning featuring simple kinematics, bi-directional motion and enlarged workspace,” *Smart Materials and Structures*, vol. 25, no. 12, article 125002, p. 15, 2016.
- [13] J. H. Kim, S. H. Kim, and Y. K. Kwak, “Development and optimization of 3-D bridge-type hinge mechanisms,” *Sensors and Actuators A: Physical*, vol. 116, no. 3, pp. 530–538, 2004.
- [14] J. Chen, C. Zhang, M. Xu, Y. Zi, and X. Zhang, “Rhombic micro-displacement amplifier for piezoelectric actuator and its linear and hybrid Model,” *Mechanical Systems and Signal Processing*, vol. 50-51, pp. 580–593, 2015.
- [15] Q. Xu and Y. Li, “Analytical modeling, optimization and testing of a compound bridge-type compliant displacement amplifier,” *Mechanism and Machine Theory*, vol. 46, no. 2, pp. 183–200, 2011.
- [16] M. Ling, J. Cao, M. Zeng, J. Lin, and D. J. Inman, “Enhanced mathematical modeling of the displacement amplification ratio for piezoelectric compliant mechanisms,” *Smart Materials and Structures*, vol. 25, no. 7, article 075022, p. 11, 2016.
- [17] S. Shao, M. Xu, S. Zhang, and S. Xie, “Stroke maximizing and high efficient hysteresis hybrid modeling for a rhombic piezoelectric actuator,” *Mechanical Systems and Signal Processing*, vol. 75, pp. 631–647, 2016.
- [18] H. Kim and D. G. Gweon, “Development of a compact and long range $XY\theta_z$ nano-positioning stage,” *Review of Scientific Instruments*, vol. 83, no. 8, article 085102, p. 8, 2012.
- [19] Y. Li, J. Huang, and H. Tang, “A compliant parallel XY micromotion stage with complete kinematic decoupling,” *IEEE Transactions on Automation Science and Engineering*, vol. 9, no. 3, pp. 538–553, 2012.
- [20] W.-L. Zhu, Z. Zhu, P. Guo, and B.-F. Ju, “A novel hybrid actuation mechanism based XY nanopositioning stage with totally decoupled kinematics,” *Mechanical Systems and Signal Processing*, vol. 99, pp. 747–759, 2018.
- [21] C. X. Li, G. Y. Gu, M. J. Yang, and L. M. Zhu, “Design, analysis and testing of a parallel-kinematic high-bandwidth XY nanopositioning stage,” *Review of Scientific Instruments*, vol. 84, no. 12, article 125111, p. 12, 2013.
- [22] W. L. Zhu, Z. Zhu, Y. Shi, X. Wang, K. Guan, and B. F. Ju, “Design, modeling, analysis and testing of a novel piezo-actuated XY compliant mechanism for large workspace nanopositioning,” *Smart Materials and Structures*, vol. 25, no. 11, article 115033, p. 18, 2016.



Hindawi
Submit your manuscripts at
www.hindawi.com

